analytical chemistry

pubs.acs.org/ac Article

Broad-Band Spectrum, High-Sensitivity Absorbance Spectroscopy in Picoliter Volumes

Julie Probst, Philip Howes, Paolo Arosio, Stavros Stavrakis,* and Andrew deMello*

Cite This: *Anal. Chem.* 2021, 93, 7673−7681 Read Online

ACCESS | Metrics & More | Article Recommendations | Supporting Information

ABSTRACT: Picoliter-volume droplets within segmented flows can be probed in a rapid and efficient manner using optical detection methods. To date, however, most detection schemes for droplet content analysis have relied on the use of time-integrated fluorescence measurements. Despite its undoubted utility, the implementation of absorbance-based detectors is particularly challenging due to the reduced optical path lengths that are characteristic of microfluidic systems and deleterious scattering at droplet−oil interfaces. Unsurprisingly, efforts to develop sensitive absorbance-based detection schemes for the interrogation of rapidly moving droplets have primarily focused on ensuring adequate analytical sensitivity and, to date, have been exclusively limited to single-wavelength measurements. To address this limitation, and expand the information content associated with absorbance measurements on-chip, we herein describe a detection scheme for the extraction of broad-band absorbance spectra from pL-volume droplets with high sensitivity. The combination of a confocal optical system (that confines incident light to a reduced detection volume) and a postprocessing algorithm (that effectively removes the contribution of the carrier oil from the extracted spectra) engenders significant improvements in signal-to-noise ratios. Our system is initially calibrated by acquiring absorbance spectra from aqueous solutions of fluorescein isothiocyanate. These measurements confirm both excellent linearity over the studied range (from 0 to 100 μM) and a concentration limit of detection of 800 nM. The methodology is then used to monitor the salt-induced aggregation of gold nanoparticles with millisecond time resolution. This approach for small-volume absorbance spectroscopy allows for both high-throughput and high-information content measurements in subnanoliter volumes and will be highly desirable in a wide variety of bioanalytical applications where sensitivity and throughput are priorities.

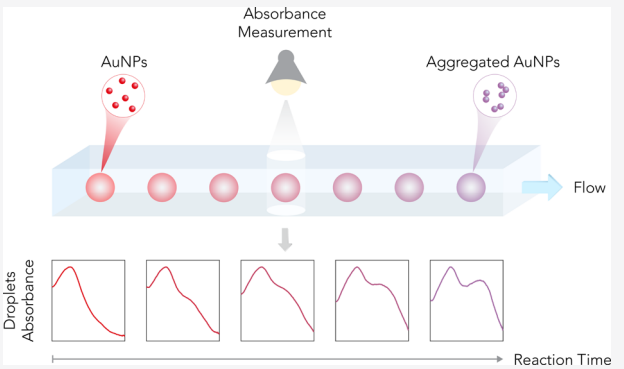

INTRODUCTION

Despite the fact that absorption spectroscopy is one of the most widely used optical techniques for the analysis of macroscopic samples, its implementation and use within microfluidic environments are far less common. Indeed, fluorescence-based detection methods remain the predominant choice within small-volume systems due to their exquisite sensitivity and selectivity, noninvasive nature, and low mass/concentration limits of detection. However, the vast majority of (both synthetic and natural) molecules are nonfluorescent and thus detection must be accomplished through chemical modification with an appropriate extrinsic fluorophore, adding significantly to assay complexity and introducing potential interferences to the analytical signal. In contrast, UV−visible absorbance spectroscopy is a pervasive, label-free method able to quantitatively analyze almost all organic molecules exhibiting some degree of conjugation and does not suffer from photobleaching or quenching effects that frequently hamper time-integrated fluorescence techniques. Despite the undoubted utility of absorbance-based detection in a wide variety of experimental scenarios, its implementation in microfluidic systems is encumbered by the fact that optical path lengths are typically between 2 and 3 orders of magnitude less than those encountered on the macroscale (i.e., ten to a hundred microns). Such abridged path lengths are almost always unavoidable, yield proportionally weaker absorbance signals, and thus significantly compromise both analytical sensitivity and limits of detection.

Early attempts to improve the sensitivity of absorbance measurements within microfluidic systems (while ensuring that detector bandwidths are not compromised) focused on the development of multireflection flow cells.[1,2] For example, Moosavi et al. pioneered the use of integral aluminum mirrors to guide light along the length of the microchannel, reporting a 5- to 10-fold increase in sensitivity.[1] Miniaturizing the flow cell geometries in all but one dimension has also been exploited as

Received: February 8, 2021
Accepted: May 6, 2021
Published: May 19, 2021

https://doi.org/10.1021/acs.analchem.1c00587
Anal. Chem. 2021, 93, 7673−7681

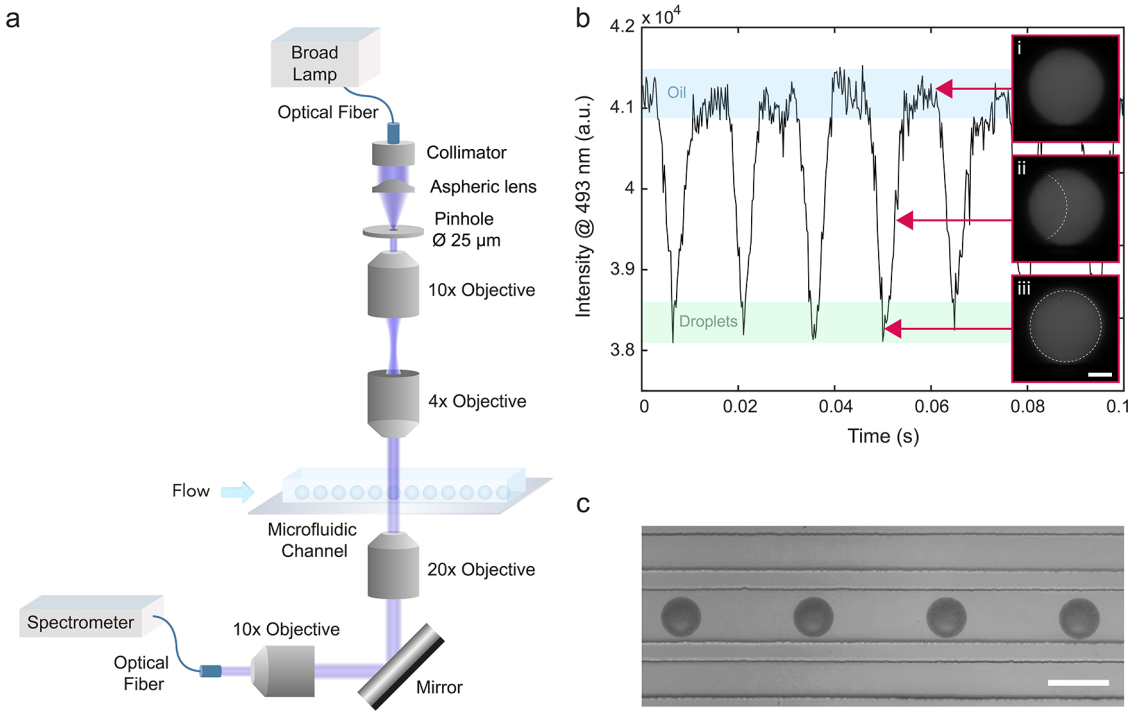

Figure 1. (a) Schematic of the optofluidic platform. A high-intensity broad-band light source is collimated, and the circular area of a 25 μm pinhole is subsequently imaged onto the microfluidic channel, yielding a 75 μm diameter circular detection area. The microfluidic channel is positioned so that each droplet is aligned within the detection area. Light exiting the channel is collected and focused onto an optical fiber connected to a fast spectrometer. Spectra were recorded at 4500 Hz with a 50 μs acquisition time. (b) Time trace of the transmitted light at 493 nm for a solution of FITC at 100 μM reporting individual droplets at a frequency of approximately 70 Hz. The insets show bright-field images corresponding to the detection area in between two droplets (i), when a droplet is partially visible (ii) and when a droplet is perfectly aligned (iii), with red arrows indicating the corresponding signal on the time trace. Dotted white lines highlight the contour of the droplet. The scale bar is 25 μm. (c) Bright-field image of the microfluidic channel with droplets containing ink for better visibility. The scale bar is 100 μm.

a way to efficiently collect light traveling along the direction of flow, hence reducing the footprint of the device while retaining an adequate optical path length.[3] Direct integration of photodetectors in the microfluidic device can also be used to bypass the need to couple transmitted light toward an external detector. Indeed, such an approach has been used for the sensitive detection of BSA at concentrations as low as 15 nM but at the expense of greatly increased manufacturing complexity and cost.[4] It is significant to note that broad-band absorbance spectra from a 13 μM methylene blue solution have been obtained in a single-pass manner with a path length of only 28 μm, using a multilayer chip composed of an elastomeric valve to switch between a reference and a sample channel.[5] Alternatively, cavity-enhanced absorption spectroscopy can be used to increase sensitivity when probing small-volume samples. For example, two high-reflectivity mirrors can be placed on each side of the detection channel to form an optical cavity in which light is reflected multiple times. Such an approach has been shown to result in a 28 times increase in the effective path length and an enhancement of the sensitivity of about 5 times.[6,7]

Over the last two decades, droplet-based microfluidic systems have become a dominant tool in high-throughput chemical and biological experimentation.[8−10] Briefly, droplets may be generated within microfluidic channels at rates of up to hundreds of kHz, with the user being able to exert exquisite control over droplet size, velocity, and composition.[11−13] Unsurprisingly, much of the power of droplet-based microfluidic tools stems from the ability to optically interrogate droplet contents in a sensitive and high-throughput manner. To this end, a wide variety of sensitive optical detection methods, including fluorescence,[14] surface-enhanced Raman (SERS),[15] surface-enhanced resonance Raman scattering (SERRS),[16] photothermal spectroscopy,[17] time-resolved fluorescence,[18] fluorescence anisotropy,[19] and infrared spectroscopy,[20] have been successfully integrated within droplet-based microfluidic systems.[21,22] Absorbance-based detectors have also been used to probe droplets in microfluidic systems. That said, the majority of these studies have focused on the interrogation of relatively large droplets (with diameters larger than 200 μm) produced at low frequencies (1−2 Hz) and at single wavelengths.[23−25] Unsurprisingly, to mitigate the limitations associated with short optical path lengths, the same strategies used for continuous-flow systems have been applied to segmented-flow platforms, namely, extended path length geometries,[26] direct integration of optical components,[27] and cavity-enhanced approaches.[28] Additionally, in contrast to continuous-flow systems, the curved interface of droplets creates undesirable scattering, and the presence of the carrier oil phase usually dampens the signal when measurements are integrated over several droplets. To mitigate this issue, Deal and Easley developed a lock-in detection approach based on alternating reference and sample droplets, enabling a limit of detection (LOD) of 500 nM (for bromophenol blue) with a path length of only 27 μm but at the expense of unacceptably low droplet generation rates (<10 Hz).[29] More recently, we showed that the combination of a continuous referencing approach, an extended path length (that stretches droplets through a constriction), and embedded liquid waveguides enabled absorbance measurements of pL-volume

https://doi.org/10.1021/acs.analchem.1c00587
Anal. Chem. 2021, 93, 7673−7681

droplets with a detection limit of 400 nM for fluorescein.[26] Moreover, and through the direct integration of on-chip optical fibers, Gielen et al. described an absorbance-activated sorting platform with a 50 μm path length and a limit of detection of 10 μM WST-1 formazan, which is sufficient for sorting individual droplets at 100 Hz based on a specified threshold.[30] Alternatively, a quasi-path length-independent approach recently introduced by Maceiczyk and co-workers, termed differential detection photothermal interferometry (DDPI), was successfully applied to quantify absorbance signals in fL-volume droplets at frequencies exceeding 10 kHz.[17] Although the aforementioned approaches have achieved low detection limits, they lack the broad-band character of conventional absorption spectroscopy. While this can be tolerated in certain applications, access to the entire visible spectrum is highly advantageous for extracting information from multicomponent systems. Surprisingly, there have been only two studies describing the application of broad-band absorption spectroscopy to the analysis of droplets within microfluidic systems.[28,31] Interestingly, in both, there is a clear trade-off between achievable sensitivity and throughput. Neil et al. leveraged a cavity-enhanced optical system to acquire broad-band absorbance spectra from flowing droplets, with an optical path length of 320 μm.[28] The authors reported an LOD of 1.4 μM for a solution of K_2IrCl_6 measured in a continuous-flow format and also demonstrated broad-band absorption spectra from 6 μL for flowing slugs with a frequency approaching 0.2 Hz. In another study, Mao et al. extracted broad-band absorbance spectra from droplets to study reaction kinetics,[31] but sensitivity limitations of the detection system restricted the application to concentrations (of Rhodamine 6G) above 100 μM.

A significant number of applications, ranging from enzyme kinetics to nanomaterial synthesis, are best investigated when complete spectral information is available. Accordingly, there is an unmet need to generalize broad-band absorbance detection schemes into the toolbox of droplet-based microfluidics. To address this need, we herein demonstrate the acquisition of complete absorbance spectra from single pL-volume droplets with a limit of detection of 800 nM for fluorescein isothiocyanate (FITC). To reconcile the short optical path lengths representative of microfluidic systems with the high sensitivity and low limits of detection of conventional spectrometers, our methodology centers on three key aspects. First, incident light is confined to a region that closely matches the size of the transiting droplets, thus minimizing contributions from stray light. Second, a fast spectrometer is used to acquire spectra using integration times as short as 50 μs. Third, a postprocessing algorithm efficiently filters out optical contributions of the continuous oil phase from the absorbance spectra, enhancing signal-to-noise (S/N) ratios through averaging a large number of spectra. Using this methodology, we demonstrate the acquisition of broad-band absorbance spectra from pL-volume droplets containing different concentrations of FITC, with a concentration detection limit of 800 nM. To highlight the utility of our approach, we additionally investigate and probe the kinetics of salt-induced gold nanoparticle aggregation through changes in the broad-band absorbance spectrum.

MATERIALS AND METHODS

Absorption Spectroscopy. Absorbance measurements were performed using a custom-built optical spectrometer, as shown in Figure 1a. Briefly, a broad-band high-intensity liquid guide-coupled light source (Medium Power Xenon Arc Lamp, Newport, Darmstadt, Germany) was collimated using a fused silica collimator (Newport, Darmstadt, Germany) and focused onto a 25 μm diameter pinhole (P25S Mounted Precision Pinhole, Thorlabs, Germany) using an aspheric lens (A240TM-A lens, Thorlabs, Dachau, Germany). Alternatively, a white LED lamp consisting of six solid-state light sources (SPECTRA X light engine, Lumencor, Beaverton) was also used as the broad-band light source in some experiments and was collimated using a fiber collimator (F950SMA-A 473, Thorlabs, Dachau, Germany). The pinhole was then imaged into the microfluidic channel using a Plano N 10 × NA 0.25 objective lens followed by a Plano N 4 × NA 0.1 (Olympus, Tokyo, Japan) to yield a 200 pL detection volume. The microfluidic chip was placed on a precision x−y stage (Mad City Laboratories, Maddison) used to align the channel with the detection area. Light transmitted through the microchannel was collected by a Plan Fluor ELWD 20 × NA 0.45 objective (Nikon, Tokyo, Japan), reflected by a mirror and coupled into an optical fiber using a Plano N 10 × NA 0.25 objective. The other end of the fiber was connected to an Ocean FX-XR1 spectrometer (Ocean Insight, Rostock, Germany) featuring a 200 μm entrance slit. The continuous and discrete phases were loaded into 5 mL and 100 μL gastight syringes (Hamilton AG, Bonaduz, Switzerland), respectively. Fluid delivery was performed using neMESYS high-precision syringe pumps (Cetoni GmbH, Korbussen, Germany) connected to the microfluidic inlets via a Tygon tubing (Cole Palmer, Hanwell, U.K.).

For the FITC calibration experiment involving serial dilutions, the oil flow rate was maintained at 6 μL/min and the total aqueous flow rate (i.e., PBS buffer + FITC) was set at 0.4 μL/min. Under these conditions, droplets were generated at a frequency of about 70 Hz with a mean droplet volume of 95 pL. For reference measurements, droplets containing PBS buffer were generated at a rate of 70 Hz and 50 000 spectra were acquired over a period of 11.11 s. The same number of spectra were used for sample measurements, where droplets of different FITC concentrations were generated on-chip by mixing different ratios of PBS and FITC stock solution (100 μM). Each measurement was averaged over 770 droplets, yielding a total sample volume of approximately 70 nL. Data from microfluidic experiments were compared with measurements using a conventional spectrophotometer (Fluoromax, HORIBA Scientific, Northampton, U.K.) incorporating a 1 cm optical path length cuvette and using 1 mL of sample.

For AuNP aggregation experiments, the oil and the total aqueous (water, NaCl solution, and AuNP solution) flow rates were set at 6 and 0.45 μL/min, respectively. Under these conditions, the droplet generation frequency was 90 Hz and the mean droplet volume was 80 pL. Droplets containing water were used as a reference when probing AuNP solution droplets, with reference droplets containing the same salt concentration as used in the sample measurement. Salt concentration was controlled by varying the ratio of the individual aqueous flow rates while keeping the total flow rate constant.

Data Acquisition and Processing. Spectra acquisition was performed using OceanView 2.0 spectroscopy software (Ocean Insights, Rostock, Germany) in burst-mode, with a dark measurement being subtracted prior to the start of each experiment. Burst-mode operation allows for a maximum

https://doi.org/10.1021/acs.analchem.1c00587
Anal. Chem. 2021, 93, 7673−7681

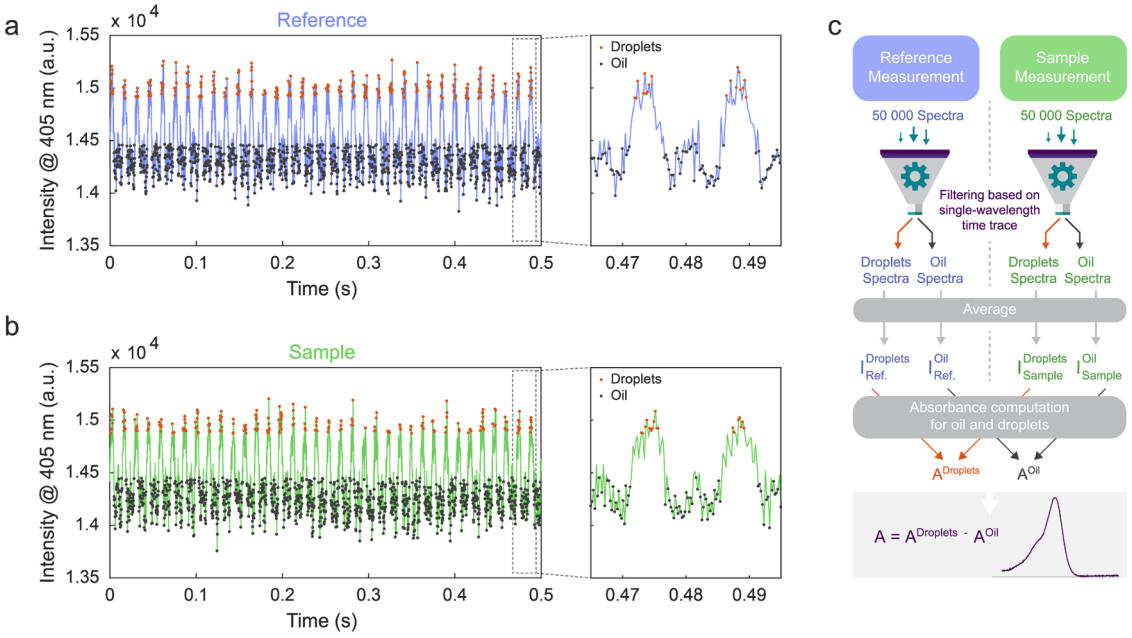

Figure 2. Workflow associated with data processing. Time traces report the intensity of transmitted light at 405 nm extracted from broad-band transmission spectra when a train of droplets passes through the detection area for (a) reference measurements (droplets containing PBS buffer) and (b) sample measurements (droplets containing 100 μM FITC). At this wavelength, the oil absorbs more strongly than the droplet. Two thresholds are applied for the selection of data points that correspond to transmitted light through the droplets (orange circles) and the oil (gray circles). These serve to cluster the data sets between broad-band transmission spectra of the droplets and oil, for both the reference and sample data sets (see the main text for details). The right panels in (a) and (b) show time traces over a period of 30 ms (highlighted by the gray rectangle in the left panel). (c) Flowchart describing the data analysis procedure. For both reference and sample measurements, 50 000 spectra are clustered into droplet and oil subsets as determined by the time traces in (a) and (b). Each subset then yields an average broad-band spectrum. The calculated absorbance spectrum involves contributions from both the droplets and the oil of the reference and the sample. This is equivalent to subtracting a background absorbance contribution of the oil to the absorbance obtained from droplets only.

acquisition rate of 4500 scans per second by using the onboard buffer-memory of the spectrometer to store spectra in real time. For all experiments, we used an integration time of 50 μs per spectrum and recorded 50 000 consecutive spectra per measurement. Each set of measurements was postprocessed using a custom MATLAB script, as summarized in Figure 2c. First, data sets were processed to select spectra that correspond to the oil and spectra that correspond to the droplets. Filtering was based on the single-wavelength time trace of light transmitted at 405 nm, as shown in Figure 2a,b. Two thresholds were used to select data points corresponding to the light transmitted through the droplets and light transmitted through the oil, respectively. This served to cluster data sets between broad-band transmission spectra from the droplets and from the oil, for both the reference and sample data sets. All spectra from each subset were then averaged to yield the average transmitted spectra of the oil and droplets from a reference measurement, i.e., $I^{\text{oil}}_{\text{reference}}$ and $I^{\text{droplets}}_{\text{reference}}$, and from a sample measurement, $I^{\text{oil}}_{\text{sample}}$ and $I^{\text{droplets}}_{\text{sample}}$ (Figure S1a). The absorbance of a sample droplet can then be calculated by subtracting absorbance spectra of light transmitted through the oil phase A^{oil} from absorbance spectra of droplets A^{droplets} (Figure S1b,c). Since the absorbance of the oil will be constant, the subtracted term here accounts for any fluctuation in the light intensity that occurs between reference and sample measurements,[25] i.e.

$$A(\lambda) = A(\lambda)^{\text{droplets}} - A(\lambda)^{\text{oil}} = -\log_{10}\left(\frac{I^{\text{droplets}}_{\text{sample}}(\lambda)}{I^{\text{droplets}}_{\text{reference}}(\lambda)}\right) + \log_{10}\left(\frac{I^{\text{oil}}_{\text{sample}}(\lambda)}{I^{\text{oil}}_{\text{reference}}(\lambda)}\right) = \varepsilon\lambda cl \quad (1)$$

Microfluidic Device Fabrication. Microfluidic devices were fabricated in polydimethylsiloxane (PDMS) following standard soft lithographic procedures, with the main observation being made from a thin membrane-like layer of PDMS. Thicker PDMS slabs for inlet and outlet areas allowed for the easy connection of the tubing. Briefly, microfluidic channel patterns were designed using AutoCAD 2018 (Autodesk, San Rafael) and printed onto high-resolution photolithographic masks (Micro Lithography Services Ltd., Chelmsford, U.K.). An SU-8 master mold with a height of 50.2 μm was fabricated via standard photolithography. Following its fabrication, the SU-8 mold was exposed to chlorotrimethylsilane (Sigma-Aldrich, Buchs, Switzerland) vapor for at least 5 h in a desiccator at a pressure of 150 mbar to aid subsequent removal of PDMS. A thin layer of 10:1 (wt/wt) mixture of PDMS base to curing agent (Sylgard 184; Dow Corning, Midland) was degassed in a desiccator for 60 min, spin-coated (800 rpm for 1 min) on the master mold, and cured for 45 min at 70 °C. PDMS slabs were then bonded onto the inlet and outlet regions using an air-plasma (EMITECH K1000X, Quorum Technologies, East Sussex, United Kingdom). Curing was continued for at least 30 min at 70 °C to strengthen the

https://doi.org/10.1021/acs.analchem.1c00587
Anal. Chem. 2021, 93, 7673−7681

bonding of the PDMS slabs. The thin PDMS-membrane layer together with the PDMS slabs was then peeled from the wafer and diced to form individual devices. Inlets and outlets were formed at the desired locations using a hole puncher (Syneo, Florida). Finally, the individual devices were bonded via air-plasma to PDMS-covered glass coverslips. Two minutes after bonding, a 5 vol % solution of (tridecafluoro-1,1,2,2-tetrahydrooctyl)trichlorosilane (ABCR-Chemicals, Karlsruhe, Germany) in HFE 7500 Novec oil was injected into the channels to render the internal surfaces hydrophobic and left for a period of 5 min. Channels were then rinsed with pure HFE oil, and devices were left on a hot plate at 120 °C for at least 2 h before use.

Materials and Reagents. The oil phase consisted of a mixture of two parts HFE 7500 Novec fluorinated oil containing 1.25% fluoro-surfactant (RAN Biotechnologies, Beverly) and one part 3,5-bis(trifluoromethyl)bromobenzene (ABCR-chemicals, Karlsruhe, Germany). The latter was used to create transparent emulsions via refractive index matching.[32] The refractive index of the fluorinated oil is 1.29, while the refractive index of 3,5-bis(trifluoromethyl)bromobenzene is 1.427. Therefore, a ratio of 1:2 (fluorinated oil: 3,5-bis(trifluoromethyl)bromobenzene) yields a refractive index of 1.33, matching that of the aqueous droplets. A stock solution of 100 μM fluorescein isothiocyanate (Sigma-Aldrich, Buchs, Switzerland) was prepared in phosphate-buffered saline (PBS 1x, Gibco, Thermo Fisher Scientific, Switzerland). A AuNP colloidal solution (BBI Solutions, Newport, U.K.) containing 15 nm diameter nanoparticles was used as received. Alternatively, a concentrated solution of AuNPs was prepared by spinning down 1 mL of this solution for 8 min at 13 000 rpm, then discarding 500 μL of the clear supernatant, and rehomogenizing the solution using a vortex mixer. Purified water (Milli-Q, Merck Millipore, Burlington) was used for on-chip dilution of the AuNP solution. To induce aggregation of the AuNPs, a 500 or 250 mM saline solution of NaCl (Sigma-Aldrich, Buchs, Switzerland) was prepared in purified water.

RESULTS AND DISCUSSION

Strategy and Working Principle. Our initial strategy focused on minimizing the scattered light that travels through droplets and onto the detector, causing a decrease in the overall sensitivity. As previously noted, integrated optical waveguides aid in coupling light into the microfluidic device and have been used in a number of schemes for absorbance measurements in droplets.[27,30,33] However, the fact that the geometry of the microfluidic channels must accommodate the waveguides adds complexity to the entire design. In addition, the use of a waveguide means that detection may be performed at only one single position along the microfluidic channel, unless additional waveguides and detectors are integrated. The ability to interrogate droplet contents at different locations across the chip is critical in many important applications, most notably in the study of reaction kinetics.[34] The optical setup presented in Figure 1a serves to shape the incident light of a high-intensity broad-band source into a defined circular area with a size comparable to that of the droplets. The pinhole (25 μm diameter) was imaged onto the sample using a microscope objective lens (4×, NA 0.1) to create a localized detection volume in the sample. Due to its low NA, its focal length is large enough to project the pinhole inside the microfluidic channel while accommodating the finite thickness of the PDMS substrate (5 mm at the inlets and outlets). Transmitted light was collected by a second objective (NA 0.45). A larger numerical aperture allows the collection of photons from a restricted depth of field, and it is advantageous if this matches the droplet diameter since more light probes the sample. In general, the numerical apertures of both objectives used were judged to provide the best possible combination of high collection efficiency and confocal depth of field. Such an approach enables the light path to travel only through the droplet volume, minimizing any stray light contributions. In addition, absorbance spectra can then be collected at any location along the channel by simply translating the entire device, enabling precise spatiotemporal mapping of reactions.

Small droplets moving at high linear velocities impart an additional challenge to the collection of broad-band absorption spectra. In the case of single-wavelength measurements, fast and sensitive detectors such as photomultiplier tubes can be used to collect photons on a time scale that matches the frequency of the droplet production. To acquire broad-band spectra, however, a spectrometer is required. If the integration (acquisition) time of the spectrometer is longer than the transit time of a droplet through the optical probe volume, averaging of several droplets into a single measurement will necessarily include a contribution of the carrier phase, which significantly reduces the transmitted signal. For this reason, almost all studies reporting absorbance detection in droplet-based microfluidic systems have utilized large droplets (nL–μL volumes) and low generation frequencies (<2 Hz). In the current study, we leveraged microsecond integration times to overcome this issue and effectively filter out the oil contribution from the overall signal. To optimize signal-to-noise ratios (SNRs), the intensity of the incident light was maximized to ensure that the signal detected by the spectrometer was close to its saturation level. The use of a high-power xenon light source enables the operation of the spectrometer at very short integration times (50 μs) while working close to saturation. Such short integration times allow droplets to be effectively "sliced" into discrete spectra, thus enabling the averaging of a large number of spectra. Such a strategy proved to be highly efficient in reducing noise and enabled the extraction of full absorbance spectra with excellent SNR.

Data Processing. Data sets were clustered into subsets corresponding to "droplets-only" or "oil-only" based on the transmitted intensity at 405 nm. To achieve an identical clustering efficiency for both reference and sample droplets across different concentrations, the wavelength used to distinguish droplets from oil was fixed regardless of the content of the droplet. For example, at 405 nm, the fluorinated oil has a slightly higher absorbance than the aqueous phase, which allows discrimination of droplets from the oil, regardless of the droplet sample concentration. In this regard, we introduce two parameters that correspond to the number of spectra included in the oil (P) and droplet (Q) subsets. These parameters can be fine-tuned after visual inspection of the single-wavelength time trace at 405 nm, as shown in Figure 2a,b. An example of the intermediate phases of the computation is included in Figure S1. In this way, we ensure that the maximum number of spectra is included in each sub-data set while achieving optimal differentiation between the oil and droplet signals. These parameters can be modified depending on the integration time used during experimentation, as well as the flow rate used. For example, a higher oil flow rate will mean that more spectra will contain oil only

https://doi.org/10.1021/acs.analchem.1c00587
Anal. Chem. 2021, 93, 7673−7681

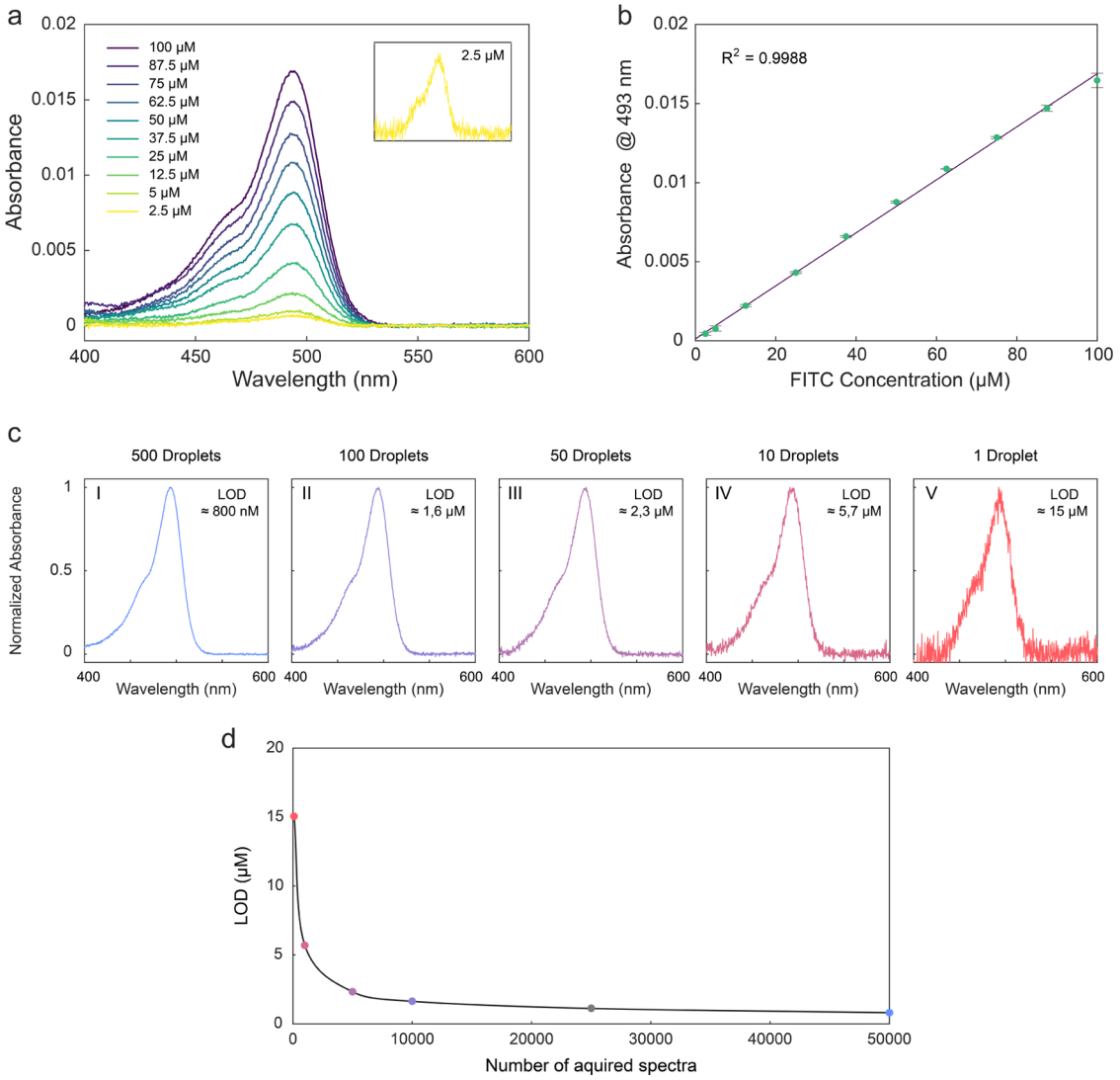

Figure 3. (a) Absorbance spectra obtained from droplets containing FITC at concentrations ranging from 2.5 to 100 μM. Each spectrum is obtained by processing a reference measurement and a sample measurement comprising 50 000 spectra each and corresponding to approximately 770 droplets. The same reference data set was used for all spectra. The inset displays an enlarged view of the lowest concentration measurement, showing the successful extraction of accurate spectral features. (b) Calibration curve based on absorbance values at 493 nm. Error bars represent the standard error from triplicate measurements. The absorbance response is linear over the entire range of concentration studied, with a high goodness of fit (R^2 = 0.9988). (c) Normalized absorbance spectra obtained when averaging decreasing numbers of droplets. Panel V confirms that a representative broad-band spectrum can be extracted from a single droplet. (d) Influence of the number of acquired spectra on the concentration LOD for FITC.

(need to increase P) and less spectra will include droplets only (need to decrease Q).

Typically, for an oil flow rate of 6 μL/min, an aqueous-phase flow rate of 0.4 μL/min, an integration time of 50 μs, and a total number of 50 000 spectra, the optimized parameters were P = 30 000 and Q = 5000. This means that 30 000 spectra were averaged for the oil contribution, while 5000 spectra were averaged for the droplet contribution. The 15 000 remaining spectra correspond to transitional instants when droplets only partially fill the detection area. These were therefore excluded.

Performance and Calibration. Due to the refractive index mismatch between the fluorinated oil (n = 1.29) and water (n = 1.33), a significant amount of light will be scattered at the droplet−oil interface. While not necessarily problematic in single-wavelength detection schemes, where a signal spike in the light intensity is seen at the droplet/oil interface, this phenomenon becomes far more problematic in the case of a full-spectrum acquisition. Indeed, such scattering induces a background signal that enhances and rounds the baseline (Figure S3). In some cases, the scattering background is so strong that it overlaps and pollutes the absorbance spectrum of the species under investigation (Figure S3b−d). To negate this issue, the reactive index of the oil is matched to that of the aqueous droplet by the addition of a high-refractive-index liquid into the oil.[32] Under these conditions, a flat baseline is obtained for buffer-containing droplets and nondistorted absorbance spectra obtained for sample-containing droplets (Figure S3a,c).

To characterize the performance and sensitivity of our method, we next analyzed pL-volume droplets containing various concentrations of an FITC solution (ε_{493} = 73 000 M^{-1} cm^{-1}) between 0 and 100 μM. The time traces of the transmitted light at 493 nm for each of these measurements are shown in Figure S2. On-chip dilution was performed by

https://doi.org/10.1021/acs.analchem.1c00587
Anal. Chem. 2021, 93, 7673−7681

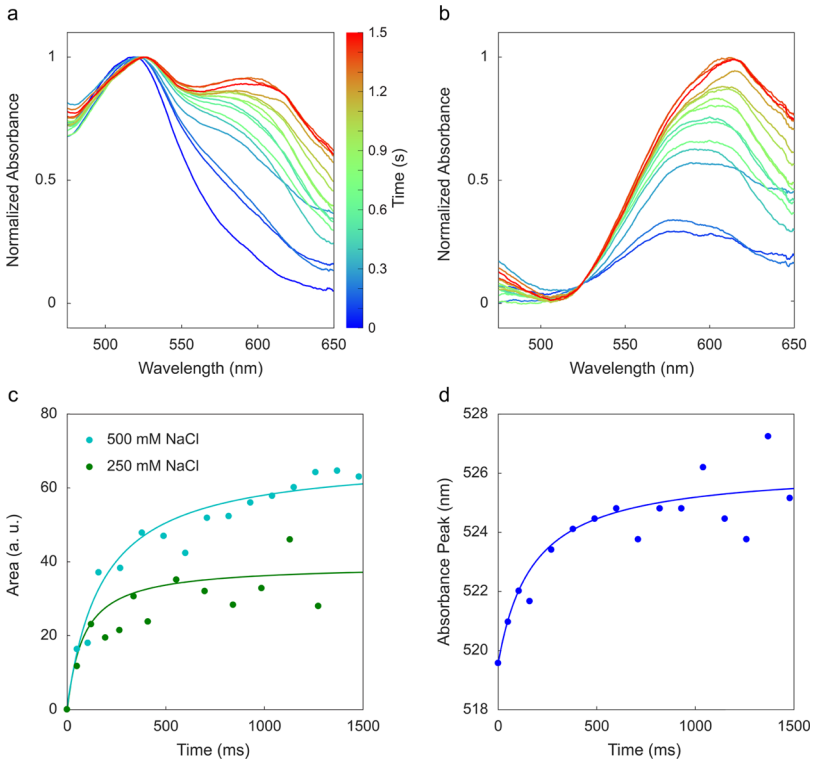

Figure 4. Salt-induced aggregation of gold nanoparticles. (a) Time evolution of the normalized absorbance spectrum of a AuNP solution after mixing with a 500 mM NaCl solution. (b) Monomer-subtracted time evolution of the absorbance spectra shown in (a). (c) Variation of the integrated area under the curve from monomer-subtracted absorbance spectra (corresponding to the contribution of the dimers) as a function of time for two salt concentrations. (d) Variation of the wavelength of the plasmonic peak as a function of time.

adjusting the ratio of a stock FITC stream and a buffer (PBS) stream, achieving a maximum dilution factor of 1:20 with high precision. Droplets containing pure PBS buffer were used as reference. Absorbance spectra resulting from droplets containing various concentrations of FITC and a corresponding calibration curve are shown in Figure 3. The variation in the absorbance value at the maximum extinction wavelength (493 nm) follows a linear relationship over the concentration range investigated (Figure 3b). The limit of detection (LOD) was determined by extrapolating the curve to a concentration that is equal to three times the standard deviation of the noise (3δ) and corresponds to 1.3×10^{-4} absorbance units or 800 nM of FITC. Moreover, to assess the spectral feature accuracy of our method, we compared representative spectra obtained from pL-volume droplets with those measured using a conventional spectrometer. Inspection of Figure S4 indicates excellent agreement between the two methods but using only 70 nL of sample with our on-chip method compared to 1 mL with the benchtop spectrometer. As noted previously, the optical path length in on-chip experiments was 50 μm, as defined by the channel height. However, the effective path length of the system is actually smaller than this value, mostly due to the droplet shape. Put simply, when a spherical droplet moves through the detection volume, the optical path length through the droplet will be reduced along its outer curved regions. Based on the Beer–Lambert law and assuming a molar extinction coefficient for FITC at 493 nm of 73 000 M^{-1} cm^{-1}, we calculated an effective path length through the droplets of 24.5 ± 0.3 μm. This is in excellent agreement with the ratio of the droplet volume (95 pL) to the detection volume of 200 pL, defined by the confocal illumination.

Importantly, we were able to obtain an absorbance spectrum from a single (reference-sample) droplet pair, with a concentration LOD of 15 μM for FITC (Figure 3c). The relationship between the number of spectra acquired (and thus the number of droplets averaged) and the LOD is depicted in Figure 3d.

Kinetics of Salt-Induced Gold Nanoparticle Aggregation. Droplet-based microfluidic systems are especially useful for studying rapid reactions due to their fast mixing capabilities, short dead times, and the correspondence between the distance traveled in the direction of flow with time.[35,36] Gold nanoparticle (AuNP) aggregation results in distinct color changes that can be leveraged in chemical and biomolecular sensing.[37] For example, colloidal solutions of AuNPs (with diameters between 5 and 20 nm) exhibit a plasmonic absorption peak around 520 nm, which confers a characteristic red color to such solutions.[38] In the presence of halide salts, AuNPs rapidly aggregate, with the solution turning a purple color, due to the shift of the absorption peak toward longer wavelengths.[39] We applied our method to monitor the kinetics of gold nanoparticle aggregation via the time evolution of the absorbance spectrum after the addition of NaCl. A schematic of the microfluidic device used for kinetic analysis is presented in Figure S5. Here, three aqueous streams converge at a flow-focusing geometry, where rapid droplet generation occurs. Droplets are subsequently driven at high speed through a winding channel section to accelerate payload mixing via chaotic advection. Subsequently, droplet velocities are reduced in the observation region by removing part of the continuous phase through flanking channels. Sequential absorbance spectra are then extracted along the observation channel and mapped to reaction time.

https://doi.org/10.1021/acs.analchem.1c00587
Anal. Chem. 2021, 93, 7673–7681

As previously noted, we observed that a difference in the refractive index between the reference and the sample droplets leads to increased background signals. Since the addition of salt into the water phase leads to a small increase of refractive index,[40] the same salt concentration was used for both the reference and sample measurements. Droplets containing the AuNPs (15 nm diameter and 2×10^{12} nanoparticles per mL), water, and a salt solution (NaCl 500 or 250 mM) were generated at the flow-focusing junction and rapidly mixed by chaotic advection along the winding channel, yielding a dead time of 50 ms. Droplet payloads were precisely controlled by varying the ratio of the incoming aqueous fluid streams. We initially recorded an absorption spectrum for the AuNP solution without the addition of salt (the monomeric spectrum at $t = 0$) and then monitored the change in absorption spectra as a function of time after induction of aggregation by the addition of NaCl up to 1500 ms (Figure 4a). As time progresses, a distinct plasmonic peak emerges at approximately 590 nm, which is attributed to interparticle plasmon coupling as the particles begin to aggregate. The short time period probed using the droplet-based microfluidic platform corresponds to a regime where aggregation behavior is dominated by the formation of short nanoparticle chains (i.e., dimers, trimers, etc.),[41] and our observations are in excellent agreement with those of Salmon and co-workers, who studied the aggregation of 30 nm diameter AuNPs via dark-field scattering and surface-enhanced Raman spectroscopy using droplet microfluidics.[32] AuNP dimers display two surface plasmon resonance peaks, one corresponding to the transversal mode that overlaps with the monomeric peak (at 520 nm for 15 nm diameter AuNPs) and another corresponding to the longitudinal mode that is red-shifted relative to the monomeric peak.[42] We note that the intensity of the peak at 520 nm was not significantly affected over the observed time scale, which is consistent with the contribution of the transversal modes of the dimers and trimers. This further confirms that we are able to observe the formation of these short multimers during the early times of aggregation (Figure S6). Figure 4b shows the (monomer-subtracted) time evolution of the absorption spectra, revealing the contribution of the dimers,[43] from which the characteristic aggregation time scale can be estimated (Figure 4c).

Under the investigated conditions, salt screens electrostatic repulsion between the surface-charged nanoparticles and aggregation occurs according to a diffusion-limited cluster aggregation (DLCA) model.[44] The predicted characteristic time of DLCA coagulation is given by

$$t = \frac{3\eta}{4kTN_0} \tag{2}$$

where η is the viscosity of the solvent, k is the Boltzmann constant, T is temperature, and N_0 is the initial concentration of nanoparticles. The calculated value of $t \approx 100$ ms is in excellent agreement with the observed experimental data (time to reach half the aggregate population; Figure 4c). Moreover, the characteristic time scale is only weakly affected by an increase of salt concentration from 250 to 500 mM, further confirming that the system is under a diffusion-limited regime (Figure 4c). Finally, we also note a small but distinct red shift of the monomeric plasmonic peak during aggregation (Figure 4d).

This proof-of-concept study demonstrates the suitability of our method for the in situ assessment of fast processes via broad-band absorbance spectroscopy. It should be noted that the use of a higher-intensity light source will allow for further improvements in the LOD by enabling faster acquisition (<50 μs) of spectra while keeping signals close to the saturation level of the spectrometer (n.b. the spectrometer used in this study enables acquisition times as short as 10 μs). Such a modification would also allow the use of increased droplet velocities and frequencies. Second, it is worth noting that there is a clear trade-off between the total acquisition time and the obtainable LOD. As discussed previously, our platform allows for the extraction of an absorbance spectrum from a single reference-sample droplet pair, with sensitivity being drastically increased by averaging over multiple droplets. For applications where the content of the droplet is uniform over multiple droplets, the acquisition of a high number of spectra is extremely valuable.

CONCLUSIONS

We have presented a novel optofluidic platform for the sensitive and high-throughput acquisition of broad-band absorbance spectra from pL-volume droplets. The innovation herein lies in two key routes to the reduction of measurement noise. First, confocal illumination effectively confines the detection area to be close to the size of the contained droplets. Second, the combination of microsecond-scale spectra acquisition with a simple postprocessing scheme enables the efficient removal of oil contributions and light source instabilities that lead to background instabilities. Importantly, our approach enables the acquisition of absorbance spectra at varying positions along a microfluidic channel, which is particularly useful for the in situ study of kinetic processes over wide time scales. Finally, the versatility of the method and the ease of fabrication of the microfluidic platform make it relevant to a wide variety of applications, such as fundamental kinetics studies and protein unfolding investigations.

ASSOCIATED CONTENT

Supporting Information

The Supporting Information is available free of charge at https://pubs.acs.org/doi/10.1021/acs.analchem.1c00587.

Intermediate computation phases for the generation of an absorbance spectrum; time traces of the transmitted light for droplets containing the reference solution and increasing concentrations of FITC; influence of the refractive index matching; comparison of our system with a benchtop spectrometer; microfluidic channel for the gold nanoparticle (AuNP) aggregation study; and time evolution of the absorbance spectra of a AuNP solution after mixing with a 500 mM NaCl solution (PDF)

AUTHOR INFORMATION

Corresponding Authors

Stavros Stavrakis − *Institute for Chemical and Bioengineering, Department of Chemistry and Applied Biosciences, ETH Zürich, 8093 Zürich, Switzerland;* orcid.org/0000-0002-0888-5953; Email: stavros.stavrakis@chem.ethz.ch

Andrew deMello − *Institute for Chemical and Bioengineering, Department of Chemistry and Applied Biosciences, ETH Zürich, 8093 Zürich, Switzerland;* orcid.org/0000-0003-1943-1356; Email: andrew.demello@chem.ethz.ch

https://doi.org/10.1021/acs.analchem.1c00587
Anal. Chem. 2021, 93, 7673−7681

Authors

Julie Probst − *Institute for Chemical and Bioengineering, Department of Chemistry and Applied Biosciences, ETH Zürich, 8093 Zürich, Switzerland*

Philip Howes − *Institute for Chemical and Bioengineering, Department of Chemistry and Applied Biosciences, ETH Zürich, 8093 Zürich, Switzerland;* orcid.org/0000-0002-1862-8395

Paolo Arosio − *Institute for Chemical and Bioengineering, Department of Chemistry and Applied Biosciences, ETH Zürich, 8093 Zürich, Switzerland*

Complete contact information is available at: https://pubs.acs.org/10.1021/acs.analchem.1c00587

Notes

The authors declare no competing financial interest.

REFERENCES

(1) Salimi-Moosavi, H.; Jiang, Y.; Lester, L.; McKinnon, G.; Harrison, D. J. *Electrophoresis* **2000**, *21*, 1291−1299.
(2) Ellis, P. S.; Lyddy-Meaney, A. J.; Worsfold, P. J.; McKelvie, I. D. *Anal. Chim. Acta* **2003**, *499*, 81−89.
(3) Sieben, V. J.; Floquet, C. F. A.; Ogilvie, I. R. G.; Mowlem, M. C.; Morgan, H. *Anal. Methods* **2010**, *2*, 484−491.
(4) Zhu, L.; Lee, C. S.; DeVoe, D. L. *Lab Chip* **2006**, *6*, 115−120.
(5) Song, W.; Yang, J. *Lab Chip* **2012**, *12*, 1251−1254.
(6) Rushworth, C. M.; Jones, G.; Fischlechner, M.; Walton, E.; Morgan, H. *Lab Chip* **2015**, *15*, 711−717.
(7) Dasgupta, P. K.; Bhawal, R. P.; Li, Y. H.; Ibraguimov, A. *Anal. Chem.* **2014**, *86*, 3727−3734.
(8) Mashaghi, S.; Abbaspourrad, A.; Weitz, D. A.; van Oijen, A. M. *TrAC, Trends Anal. Chem.* **2016**, *82*, 118−125.
(9) Teh, S. Y.; Lin, R.; Hung, L. H.; Lee, A. P. *Lab Chip* **2008**, *8*, 198−220.
(10) Schaerli, Y.; Hollfelder, F. *Mol. BioSyst.* **2009**, *5*, No. 1392.
(11) Song, H.; Chen, D. L.; Ismagilov, R. F. *Angew. Chem. Int. Ed.* **2006**, *45*, 7336−7356.
(12) Shang, L.; Cheng, Y.; Zhao, Y. *Chem. Rev.* **2017**, *117*, 7964−8040.
(13) Joensson, H. N.; Andersson Svahn, H. *Angew. Chem. Int. Ed.* **2012**, *51*, 12176−12192.
(14) Baret, J. C.; Miller, O. J.; Taly, V.; Ryckelynck, M.; El-Harrak, A.; Frenz, L.; Rick, C.; Samuels, M. L.; Hutchison, J. B.; Agresti, J. J.; Link, D. R.; Weitz, D. A.; Griffiths, A. D. *Lab Chip* **2009**, *9*, 1850−1858.
(15) Walter, A.; März, A.; Schumacher, W.; Rösch, P.; Popp, J. *Lab Chip* **2011**, *11*, 1013−1021.
(16) Cecchini, M. P.; Hong, J.; Lim, C.; Choo, J.; Albrecht, T.; deMello, A. J.; Edel, J. *Anal. Chem.* **2011**, *83*, 3076−3081.
(17) Maceiczyk, R. M.; Hess, D.; Chiu, F. W. Y.; Stavrakis, S.; deMello, A. J. *Lab Chip* **2017**, *17*, 3654−3663.
(18) Léonard, J.; Dumas, N.; Caussé, J. P.; Maillot, S.; Giannakopoulou, N.; Barre, S.; Uhring, W. *Lab Chip* **2014**, *14*, 4338−4343.
(19) Choi, J. W.; Kang, D. K.; Park, H.; deMello, A. J.; Chang, S. I. *Anal. Chem.* **2012**, *84*, 3849−3854.
(20) Chan, K. L. A.; Niu, X.; deMello, A. J.; Kazarian, S. G. *Anal. Chem.* **2011**, *83*, 3606−3609.
(21) Zhu, Y.; Fang, Q. *Anal. Chim. Acta* **2013**, *787*, 24−35.
(22) Liu, W.; wen & Zhu, Y. *Anal. Chim. Acta* **2020**, *1113*, 66−84.
(23) Srinivasan, V.; Pamula, V. K.; Fair, R. B. *Anal. Chim. Acta* **2004**, *507*, 145−150.
(24) Gielen, F.; van Vliet, L.; Koprowski, B. T.; Devenish, S. R. A.; Fischlechner, M.; Edel, J. B.; Niu, X.; deMello, A. J.; Hollfelder, F. *Anal. Chem.* **2013**, *85*, 4761−4769.
(25) Hassan, S. U.; Nightingale, A. M.; Niu, X. *Analyst* **2016**, *141*, 3266−3273.
(26) Yang, T.; Stavrakis, S.; deMello, A. *Anal. Chem.* **2017**, *89*, 12880−12887.
(27) Nightingale, A. M.; Hassan, S. U.; Makris, K.; Bhuiyan, W. T.; Harvey, T. J.; Niu, X. *RSC Adv.* **2020**, *10*, 30975−30981.
(28) Neil, S. R. T.; Rushworth, C. M.; Vallance, C.; MacKenzie, S. R. *Lab Chip* **2011**, *11*, 3953−3955.
(29) Deal, K. S.; Easley, C. J. *Anal. Chem.* **2012**, *84*, 1510−1516.
(30) Gielen, F.; Hours, F.; Emond, S.; Fischlechner, M.; Schell, U.; Hollfelder, F. *Proc. Natl. Acad. Sci. U.S.A.* **2016**, *113*, 7383−7389.
(31) Mao, Z.; Guo, F.; Xie, Y.; Zhao, Y.; Lapsley, M. I.; Wang, L.; Mai, J. D.; Costanzo, F.; Huang, T. J. *J. Lab. Autom.* **2015**, *20*, 17−24.
(32) Salmon, A. R.; Esteban, R.; Taylor, R. W.; Hugall, J. T.; Smith, C. A.; Whyte, G.; Scherman, O. A.; Aizpurua, J.; Abell, C.; Baumberg, J. J. *Small* **2016**, *12*, 1788−1796.
(33) Hengoju, S.; Wohlfeil, S.; Munser, A. S.; Boehme, S.; Beckert, E.; Shvydkiv, O.; Tovar, M.; Roth, M.; Rosenbaum, M. A. *Biomicrofluidics* **2020**, *14*, No. 024109.
(34) Hess, D.; Yang, T.; Stavrakis, S. *Anal. Bioanal. Chem.* **2020**, *412*, 3265−3283.
(35) Song, H.; Ismagilov, R. F. *J. Am. Chem. Soc.* **2003**, *125*, 14613−14619.
(36) Hess, D.; Rane, A.; deMello, A. J.; Stavrakis, S. *Anal. Chem.* **2015**, *87*, 4965−4972.
(37) Tang, L.; Li, J. *ACS Sens.* **2017**, *2*, 857−875.
(38) Bohren, C. F.; Huffman, D. R. *Absorption and Scattering of Light by Small Particles*; John Wiley & Sons, 1983.
(39) Kreibig, U.; Genzel, L. *Surf. Sci.* **1985**, *156*, 678−700.
(40) Zhao, X. Y.; Peng, Y. F.; Zhai, C. C.; Han, X. Y.; Zhang, Y. *Appl. Mech. Mater.* **2014**, *716−717*, 118−121.
(41) Zohar, N.; Chuntonov, L.; Haran, G. *J. Photochem. Photobiol., C* **2014**, *21*, 26−39.
(42) Esashika, K.; Ishii, R.; Tokihiro, S.; Saiki, T. *Opt. Mater. Express* **2019**, *9*, 1667.
(43) Kadkhodazadeh, S.; De Lasson, J. R.; Beleggia, M.; Kneipp, H.; Wagner, J. B.; Kneipp, K. *J. Phys. Chem. C* **2014**, *118*, 5478−5485.
(44) Lin, M. Y.; Lindsay, H. M.; Weitz, D. A.; Klein, R.; Ball, R. C.; Meakin, P. *J. Phys.: Condens. Matter* **1990**, *2*, 3093−3113.